water

MDPI

Article

Study on Transient Flow Characteristics of Pump Turbines during No-Load Condition in Turbine Mode Startup

Xianliang Li [1], Haiyang Dong [2], Yonggang Lu [1], Xiji Li [2] and Zhengwei Wang [1,*]

[1] Laboratory of Hydroscience and Engineering, Tsinghua University, Beijing 100190, China; 2222311050@stmail.ujs.edu.cn (X.L.); luyg@ujs.edu.cn (Y.L.)
[2] State Grid Xinyuan Shandong Weifang Pumped Storage Co., Ltd., Weifang 261051, China; haiyang-dong@sgxy.sgcc.com.cn (H.D.); xiji-li@sgxy.sgcc.com.cn (X.L.)
* Correspondence: wzw@mail.tsinghua.edu.cn

Abstract: To address the escalating demand for power grid load regulation, pumped storage power stations must frequently switch between operational modes. As a key component of such stations, the pump turbine has seen extensive research on its steady-state flow behavior. However, the intricate dynamics of its transient flow have not yet been thoroughly examined. Notably, the no-load condition represents a quintessential transient state, the instability of which poses challenges for grid integration. Under certain extreme conditions, this could result in the impairment of the unit's elements, interruption of its functioning, and endangerment of the security of the power station's output as well as the stability of the power network's operations. Thus, investigating the flow characteristics of pump turbines under no-load conditions is of significant practical importance. This paper focuses on the transient flow characteristics of a Weifang hydro-generator unit under no-load conditions, exploring the internal unsteady flow features and their underlying mechanisms. The study reveals that under no-load conditions, the runner channel is obstructed by a multitude of vortices, disrupting the normal pressure gradient within the runner and resulting in substantial hydraulic losses. Within the draft tube, a substantial reverse flow zone is present, predominantly along the walls. This irregular flow pattern within the tube generates a potent, stochastic pressure fluctuation. In addition to the interference frequencies of dynamic and static origins, the pressure pulsation frequency at each measurement point also encompasses a substantial portion of low-frequency, high-amplitude components.

Keywords: pump turbine; no-load; blade vortex; entropy generation; pressure pulsation

Citation: Li, X.; Dong, H.; Lu, Y.; Li, X.; Wang, Z. Study on Transient Flow Characteristics of Pump Turbines during No-Load Condition in Turbine Mode Startup. *Water* **2024**, *16*, 2741. https://doi.org/10.3390/w16192741

Academic Editor: Giuseppe Pezzinga

Received: 21 August 2024
Revised: 14 September 2024
Accepted: 16 September 2024
Published: 26 September 2024

1. Introduction

Pumped storage units are pivotal in addressing peak energy demands while also being adept at harnessing periods of low power consumption to store energy efficiently through the pumped storage process. This dual capability ensures the optimization of energy utilization. The method of energy storage is instrumental in stabilizing the power grid's load, thereby enhancing both the operational efficiency and the overall reliability of the grid.

However, the evolving requirements for a broader operational spectrum and swifter response times from the power grid have rendered the 'low head start' operation of these units indispensable [1]. The issue of grid connection failure during low-head startup, a consequence of no-load instability, is not uncommon among domestic power stations.

In the quest to understand no-load transient conditions, scholars worldwide have contributed valuable research. Gentner [2], for instance, presented numerical simulations coupled with PIV measurements demonstrating that under zero-load conditions, the dynamic relationship between the primary stream and the incoming reverse stream within the runner leads to the emergence of vortex formations. These vortices obstruct the

runner's flow channel, complicating the grid connection process for the unit. Meanwhile, Houde et al. [3] delved into the root causes of no-load instability in axial-flow turbines, employing a comprehensive approach that integrated experimental and numerical simulation techniques. Their study suggests that rotating stall events are closely associated with the existence of unstable vortices, not solely attributable to the runner blade's configuration or inherent traits. This significant revelation paves the way for enhancing turbine stability by refining flow dynamics, all without necessitating alterations to the blade configuration.

Li et al. [4] dedicated their work to examining the dynamic performance impacts on the runner as a result of operational head variations in the pump turbine during power generation. Their research highlights that the leading and trailing edges of the blades experience pressure fluctuations primarily driven by static and dynamic interactions, along with the vortex band effect. Within the domain of numerical investigations into the unloaded state of Francis turbines, Decaix [5] and team utilized a variety of RANS turbulence models. They compared the performance of these models to the predictions of the conventional SST k-ω turbulence model. The findings indicated that the SST-SAS model surpasses the conventional SST k-ω model in accurately representing the subtleties of pressure and velocity variations, providing a more detailed and precise portrayal of flow dynamics in unloaded conditions. Scholars like Nennemann [6] have directed their research towards the intricacies of the unsteady no-load condition, meticulously probing its potential to influence the fatigue life of Francis turbine runners. This inquiry is profoundly significant, offering insights crucial for bolstering the robustness and service duration of hydraulic turbine runners. Jiang et al. [7] delved into computational fluid dynamics, performing one-way fluid–solid coupling numerical calculations for the pump turbine's runner under a spectrum of operational settings. They adeptly charted the runner's static stress distribution under both turbine and pump operating conditions, followed by an in-depth analysis of the runner's stress distribution traits across these contrasting operational regimes. Wang [8] leveraged sophisticated dynamic mesh technology to simulate the startup procedures of reversible pump turbines, factoring in two divergent guide vane control strategies. The investigation uncovered that operational instability predominantly emanates from the interplay of dynamic and static forces within the flow channel, the pivotal actions of the guide vanes, and the swirling currents within the draft tube. These elements induce variations in the fluid forces impinging on the runner, heightening the unit's susceptibility to instability during the startup sequence and when the load is incrementally raised under partial opening conditions. Meng Qing [9] performed an extensive numerical simulation to clarify the dynamic characteristics and flow dynamics inside the pump turbine during no-load startup. The research revealed how the operation of the adjustable guide vanes affects the runner's force, the distribution of vortex cores in the flow passage, and the interaction with the 'S'-shaped performance curve. Within the field of unloaded pump turbine research, Hu [10] discovered that a runner with an alternating long and short blade design exhibited superior dynamic and static interference characteristics under no-load conditions. This design demonstrated lower pressure pulsation amplitudes and a more balanced S characteristic curve, offering a viable direction for enhancing the pump turbine's stability during off-design operations. Huang Wenlong and Bi Huili et al. [11] noted that during startup, when the pump turbine shifts to an unloaded condition with small guide vane openings and quick acceleration, a high-velocity water ring emerges in the space devoid of vanes. This phenomenon leads to a precipitous decline in flow and torque, accompanied by the emergence of numerous intricate vortex structures within the runner channel.

Expanding on these insights, this study further explores the unloaded state of the pump turbine during the initial startup phase. It primarily examines the flow field dynamics of the runner, guide vane, vaneless area, and draft tube, uncovering the linkage between the evolution of the internal flow field and pressure pulsations.

2. Research Object and Methodology

2.1. Research Object

In this study, our attention is directed towards the vertical shaft single-stage mixed-flow reversible pump turbine model from the Weifang Pumped Storage Power Station in Shandong, China. Our detailed three-dimensional simulation includes key flow elements like the volute, stay vanes, guide vanes, runner, upper crown cavity, lower ring cavity, and draft tube, as depicted in Figure 1. The fundamental parameters are presented in Table 1.

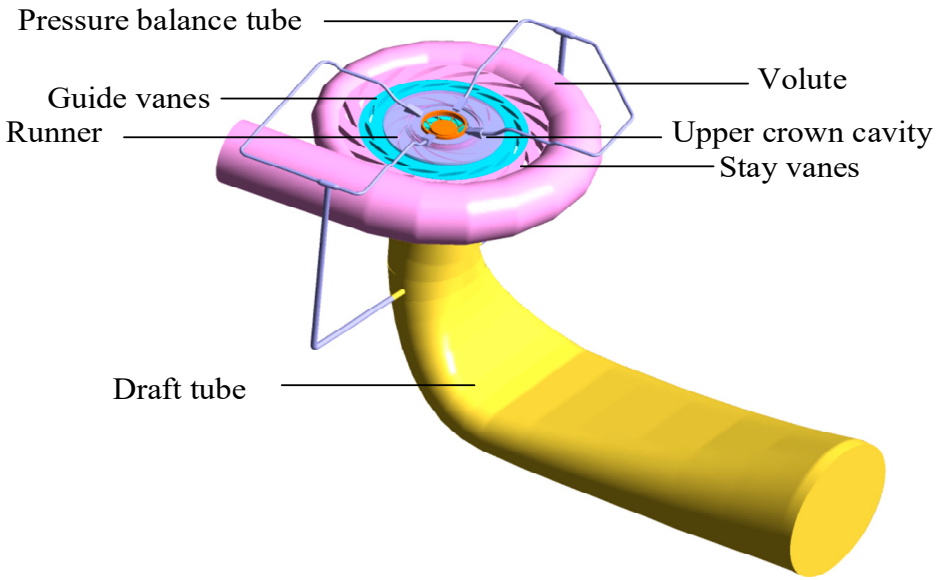

Figure 1. A 3D model has been constructed, replicating the pump turbine from the Weifang Pumped Storage Power Station.

Table 1. Key performance metrics for the vertical shaft single-stage mixed-flow reversible pump turbine.

Parameters	Value
Rated discharge	105.8 m^3/s
Rated head	326 m
Rated Speed	333.3 rpm
Rated output of turbine	306 MW
High pressure side diameter of runner	4.81 m
Installation elevation	196 m
Number of stay vanes	15
Number of guide vanes	16
Number of runner blades (long + short)	5 + 5

2.2. Mesh Subdivision

In this study, CFX software 2023 version was utilized to model the flow dynamics within a pump turbine setup. The CFD analysis encompassed components such as the volute, guide vanes, runner, draft tube, upper crown cavity, lower ring cavity, pressure balance tube, and discharge cone. The fluid regions were meshed into a grid consisting of tetrahedrons, pyramids, wedges, and hexahedrons, as shown in Figure 2.

In this study, numerical simulations of the internal flow field of a pump turbine were conducted using CFX. The fluid domains of the volute, fixed guide vanes, adjustable guide vanes, runner, draft tube, upper crown cavity, lower ring cavity, pressure balance pipe, and discharge cone were meshed using tetrahedral, pyramidal, wedge, and hexahedral elements, as shown in Figure 2. The structured and unstructured grid numbers for the volute and fixed guide vanes are approximately 2.21 million, including tetrahedral, pyramidal, and wedge elements, with five boundary layer grids set for the fixed guide vanes. The

structured and unstructured grid numbers for the adjustable guide vanes are approximately 570,000, including wedge and hexahedral elements, with five boundary layer grids set. The runner used only unstructured grids, with a grid number of 2.59 million, including pyramidal, tetrahedral, and wedge elements; the draft tube's unstructured and structured grid numbers are 1.159 million, including hexahedral and tetrahedral grids; additionally, the upper crown and lower ring cavity grid numbers are 620,000, including hexahedral and wedge grids, the pressure balance pipe grid number is 201,000, including pyramidal, tetrahedral, hexahedral, and wedge elements, and the discharge cone grid number is 716,000, including pyramidal, tetrahedral, and wedge elements. The total grid number is approximately 8.07 million.

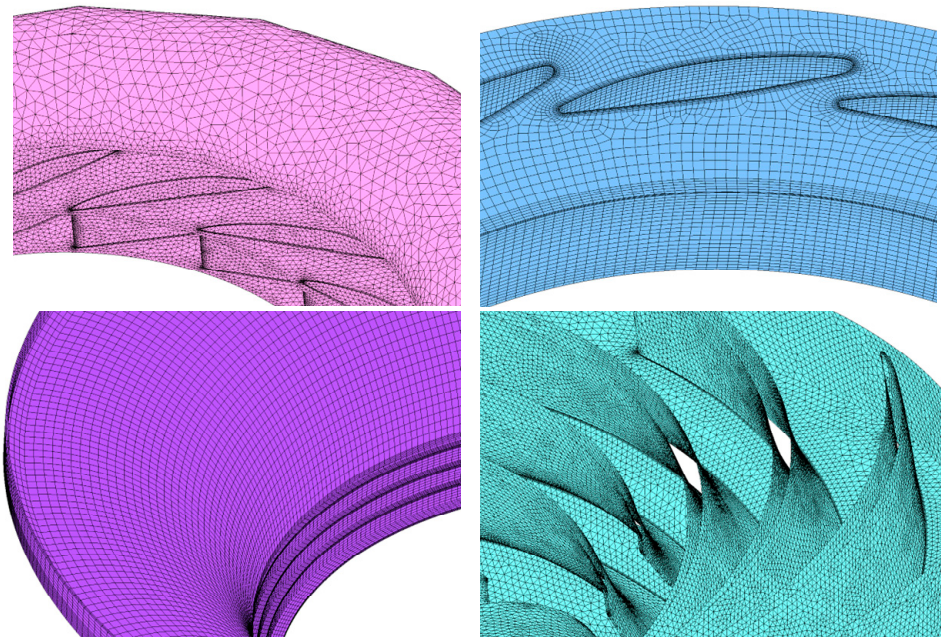

Figure 2. Part of the mesh subdivision display.

2.3. Turbulence Model and Control Equation

For this research, the Shear Stress Transport (SST) turbulence model was chosen. This model blends the k-ε and k-ω models to handle various flow field regions effectively. During the fluid flow simulation, both the mass conservation principle and the momentum conservation principle are adhered to.

The SST k-ω model encapsulates the Reynolds stress as follows:

$$v_t = \frac{\alpha_1 k}{\max(\alpha_1 w, \Omega F_2)} \tag{1}$$

$$\frac{\partial k}{\partial t} + U_j \frac{\partial k}{\partial x_j} = P_k - \beta^* \omega k + \frac{\partial}{\partial x_j}\left[(v + \sigma_k \mu_t)\frac{\partial k}{\partial y}\right] \tag{2}$$

$$\frac{\partial \omega}{\partial t} + U_j \frac{\partial w}{\partial x_j} = aS^2 - \beta^* \omega^2 + \frac{\partial}{\partial x_j}\left[(v + \sigma_w v_t)\frac{\partial \omega}{\partial x_j}\right] + 2(1 - F_1)\sigma_{\omega 2}\frac{1}{\omega}\frac{\partial k}{\partial x_i}\frac{\partial w}{\sigma x_i} \tag{3}$$

The parameter values in the model are as follows:

$$F_2 = \tanh\left[\left[\max\left(\frac{2\sqrt{k}}{\beta^* \omega^y}, \frac{500}{y^2}\frac{v}{\omega}\right)\right]^2\right] \tag{4}$$

$$P_k = \min\left(\tau_{ij}\frac{\partial U_i}{\partial x_j}, 10\beta^* kw\right) \tag{5}$$

$$F_1 = \tanh\left\{\left\{\min\left[\max\left(\frac{\sqrt{k}}{\beta^* wy}, \frac{500v}{y^2 w}\right), \frac{4\sigma_{w_2} k}{CD_{kw} y^2}\right]\right\}^4\right\} \tag{6}$$

$$CD_{k\omega} = \max\left(2\rho\sigma_{\omega 2}\frac{1}{\omega}\frac{\partial k}{\partial x_i}\frac{\partial \omega}{\partial x_i}, 10^{-10}\right) \tag{7}$$

In the above formulas, $\phi = \phi_1 F_1 + \phi_2(1 - F_1)$, $\alpha_1 = \frac{5}{9}$, $\alpha_2 = 0.44$, $\beta_1 = \frac{3}{40}$, $\beta_2 = 0.0828$, $B^* = \frac{9}{100}$, $\sigma_{k_1} = 0.85$, $\sigma_{k_2} = 1$, $\sigma_{\omega_1} = 0.5$, and $\sigma_{\omega_2} = 0.856$, where Ω represents vorticity and y represents the distance from the wall.

The turbine's hydraulic losses have a profound impact on the machinery's performance and efficiency. Gaining insights into the distribution of these losses is of practical significance for enhancing mechanical efficiency. While the pressure difference method assesses energy losses, it falls short in pinpointing the precise spatial distribution of such losses. The entropy generation method offers a clear and intuitive approach to delineate the distribution of energy losses along the fluid's path, aiding in the precise identification of loss sources and their subsequent optimization. The second law of thermodynamics underscores that entropy generation is an inherent outcome of energy transformation. Viscous forces drive the conversion of the fluid's kinetic and pressure energy into internal energy, thereby augmenting entropy. In the operational phase of the turbine, the unstable flow within regions characterized by high Reynolds numbers engenders both hydraulic losses and an increase in entropy. Utilizing the entropy generation method enables a distinct mapping of the areas where flow losses occur and facilitates the quantification of hydraulic losses within the flow field.

The system's local entropy production rate (LEPR) is a sum of two components: the direct entropy production rate (EPDR), derived from the time-averaged velocities, and the turbulent entropy production rate (EPTR), resulting from velocity fluctuations. The total entropy generation within the system is the combination of the local entropy production rate and the wall entropy production rate (EPWR), which is influenced by the presence of boundaries:

$$\dot{S}'''_D = \dot{S}'''_{\overline{D}} + \dot{S}'''_{D'} + \dot{S}'''_W \tag{8}$$

$$\dot{S}'''_{\overline{D}} = \frac{2\mu_{eff}}{T} + \frac{\mu_{eff}}{T}\left[\left(\frac{\partial \overline{\mu}_2}{\partial x_1} + \frac{\partial \overline{\mu}_1}{\partial x_2}\right)^2 + \left(\frac{\partial \overline{\mu}_3}{\partial x_1} + \frac{\partial \overline{\mu}_1}{\partial x_3}\right)^2 + \left(\frac{\partial \overline{\mu}_2}{\partial x_3} + \frac{\partial \overline{\mu}_3}{\partial x_2}\right)^2\right] \tag{9}$$

$$\dot{S}'''_{D'} = \frac{2\mu_{eff}}{T} + \frac{\mu_{eff}}{T}\left[\left(\frac{\partial \mu'_2}{\partial x_1} + \frac{\partial \mu'_1}{\partial x_2}\right)^2 + \left(\frac{\partial \mu'_3}{\partial x_1} + \frac{\partial \mu'_1}{\partial x_3}\right)^2 + \left(\frac{\partial \mu'_2}{\partial x_3} + \frac{\partial \mu'_3}{\partial x_2}\right)^2\right] \tag{10}$$

In the equation, $\dot{S}'''_{\overline{D}}$ denotes the direct entropy production rate per unit volume; $\dot{S}'''_{D'}$ signifies the turbulent entropy production rate per unit volume. The temperature, T, is set at 298 K, which is consistent throughout the analysis. $\overline{\mu}_i$ represents the time-averaged velocity component, while μ'_i denotes the fluctuating velocity component due to turbulence. The index i corresponds to the three axes of the Cartesian coordinate system (I = 1, 2, 3). μ_{eff} refers to the effective dynamic viscosity. Owing to the complexities in measuring turbulent velocity components, direct computation of the turbulent entropy production rate, $\dot{S}'''_{D'}$, triggered by velocity fluctuations, is impractical. In alignment with the principles of local entropy generation, the SST k-ω turbulence model provides a specific formula to estimate this rate, which is delineated as follows:

$$\dot{S}'''_{D'} = \beta\frac{\rho\omega k}{T} \tag{11}$$

Given the challenge of capturing turbulent velocity fluctuations, the direct computation of the turbulent entropy production rate, $\dot{S}'''_{D'}$, is not feasible. In the context of local entropy production theory, for the SST k-ω turbulence model, the calculation of the turbulent entropy production rate is articulated by the formula presented below. Within the formula, β denotes the empirical constant specific to the SST k-ω turbulence model, with a value of 0.09; ρ signifies the fluid density; ω is indicative of the turbulent vorticity frequency; and k corresponds to the turbulent kinetic energy. The vicinity of the wall experiences a pronounced velocity gradient, creating a potent wall effect, and consequently, a notable wall entropy production. To delve into the precise extent of this phenomenon, the formula for calculating the wall entropy production rate per unit area is presented as follows:

$$\dot{S}'''_{W} = \frac{\vec{\tau} \cdot \vec{v}}{T} \tag{12}$$

In the formula, $\vec{\tau}$ symbolizes the wall shear stress and $\vec{v}$ represents the velocity of the first grid layer adjacent to the wall.

By amalgamating the three distinct entropy production rates, one can ascertain their individual contributions to entropy generation, with the aggregate of these three rates constituting the overall entropy production:

$$S_{pro,\overline{D}} = \int_V \dot{S}'''_{\overline{D}} dV \tag{13}$$

$$S_{pro,D'} = \int_V \dot{S}'''_{D'} dV \tag{14}$$

$$S_{pro,W} = \int_A \dot{S}'''_{W} dA \tag{15}$$

$$S_{pro} = S_{pro,\overline{D}} + S_{pro,D'} + S_{pro,W} \tag{16}$$

Within the formula, $S_{pro,\overline{D}}$ denotes the direct entropy production; $S_{pro,D'}$ signifies the turbulent entropy production; $S_{pro,W}$ indicates the wall entropy production; and S_{pro} embodies the total entropy production of the system. The variable V represents the unit volume for integrating the entropy production rate, while A denotes the unit area for the same integration process.

2.4. Boundary Conditions, Monitoring Point Setting

In this study, the computational fluid dynamics (CFD) analysis is meticulously set up as follows: The SST turbulence model is utilized for numerical simulations, with the computational domain's reference pressure set to 1 atmosphere. The turbine's water flow enters vertically from the volute's inlet and exits the draft tube vertically [12]. The inlet boundary condition is specified by Total Pressure, and the outlet is controlled by Average Static Pressure. A no-slip condition is imposed on all wall boundaries. The unsteady simulation is initialized from the steady-state results, with a time step equivalent to a 2-degree rotation of the turbine, and the simulation spans 11 full rotation cycles [13]. Thus, the total unsteady simulation time is established at t = 1.98 s, with a time step of $\triangle$t = 0.0010 s. The dynamic interactions at the interfaces among the runner, guide vane, and draft tube are captured using the Transient Rotor Stator method, aiming for a convergence residual accuracy of 10^{-4}.

Figure 3 illustrates the strategic placement of monitoring points within the turbine. To assess the impact of downstream components on pressure pulsations in the volute, the study strategically places two monitoring points within the vaneless space, a pair at the runner, and a set of four at the draft tube. This configuration aims to provide a comprehensive assessment of the flow behavior and its interaction with the turbine's components [14].

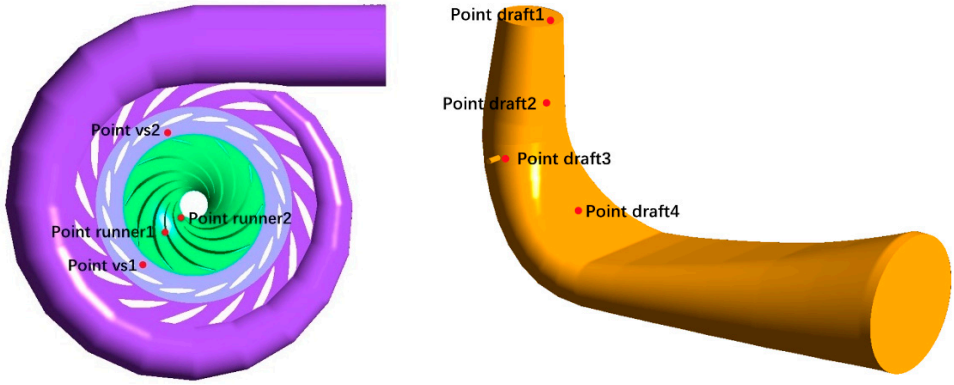

Figure 3. Distribution of monitoring points inside the turbine.

2.5. Grid Independence Verification

To mitigate the impact of grid density on numerical simulation outcomes, various grid configurations were employed for both the rated and high-head turbine scenarios at identical guide vane openings, as illustrated in Figure 4. Continuity curves were then generated to analyze the data. The results indicate that the flow rate stabilizes as the grid density increases. Balancing computational efficiency with simulation accuracy, the grid arrangement previously outlined was ultimately chosen for its optimal performance.

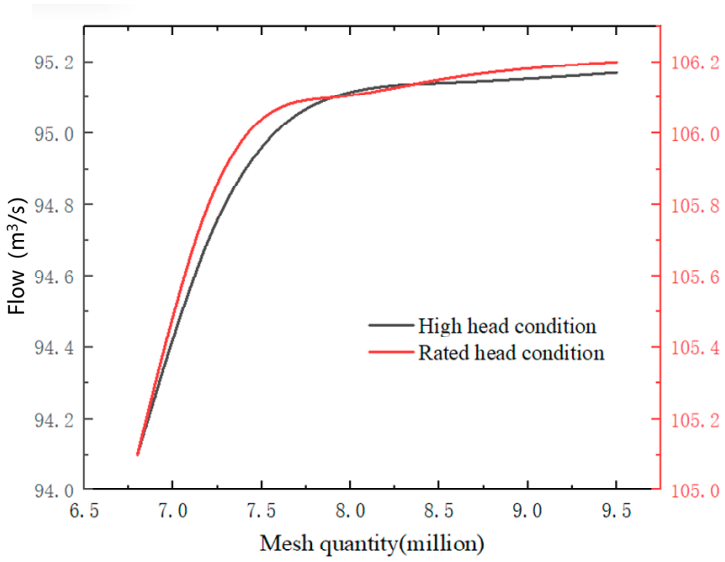

Figure 4. Mesh independence verification.

Model experiments substantiates the viability of numerical simulation techniques. As demonstrated in Table 2, the discrepancies between the model test outcomes and numerical simulation data under the rated head scenario are minimal: the flow rate deviation remains below 5%, and the rotational speed variance is within 1%, aligning with the numerical simulation projections.

Table 2. The outcomes from model experiments and numerical simulations, conducted under the specified rated head scenario, are juxtaposed.

	Flow Rate	**Rotational Speed**
Simulation	15.09 m^3/s	332 rpm
Experiment	14.62 m^3/s	330.64 rpm

3. Results and Analysis

3.1. Hydraulic Loss of Unit

Under minimal load conditions with small openings, the hydraulic losses of the internal components of the pump turbine are crucial to the equipment's performance and stability. In such scenarios, the pump turbine's operating conditions diverge markedly from those under typical loaded conditions, resulting in altered internal flow dynamics and shifts in energy conversion efficiency. The vaneless region may experience high-speed circulation and backflow, phenomena that could substantially elevate local hydraulic losses and potentially obstruct the flow path.

In these circumstances, critical turbine components like runners, guide vanes, and draft tubes encounter unique hydraulic challenges, including flow separation, vortex formation, pressure pulsations, and the risk of cavitation. To profoundly comprehend the performance of these components under no-load and minimal opening conditions, a detailed analysis of the hydraulic losses of each key component is warranted. Employing the concept of entropy generation as previously outlined, the method of entropy generation analysis becomes a critical metric for evaluating hydraulic losses. This approach primarily includes the assessment of direct, turbulent, and wall entropy generation, providing a holistic framework for gauging the efficiency and stability of the pump turbine during light load operations.

Entropy generation often coincides with the development of substantial velocity gradients, which may trigger unstable flow phenomena like flow separation, reverse flow, and vortex formation. Such events can result in a spectrum of hydraulic losses. To delve into the impact of different entropy production types on the total entropy, Figure 5 presents the output values and proportions of these distinct entropy categories. It is clear that the entropy generation within the system is primarily influenced by turbulent velocities and wall effects, with turbulent entropy generation being the most substantial contributor in both the guide vane and the runner's draft tube. In combination, the contributions of turbulent and wall entropy generations exceed 99% of the total entropy production. Direct entropy generation, being minimal at less than 1%, is negligible and thus not depicted in Figure 4 for the sake of clarity.

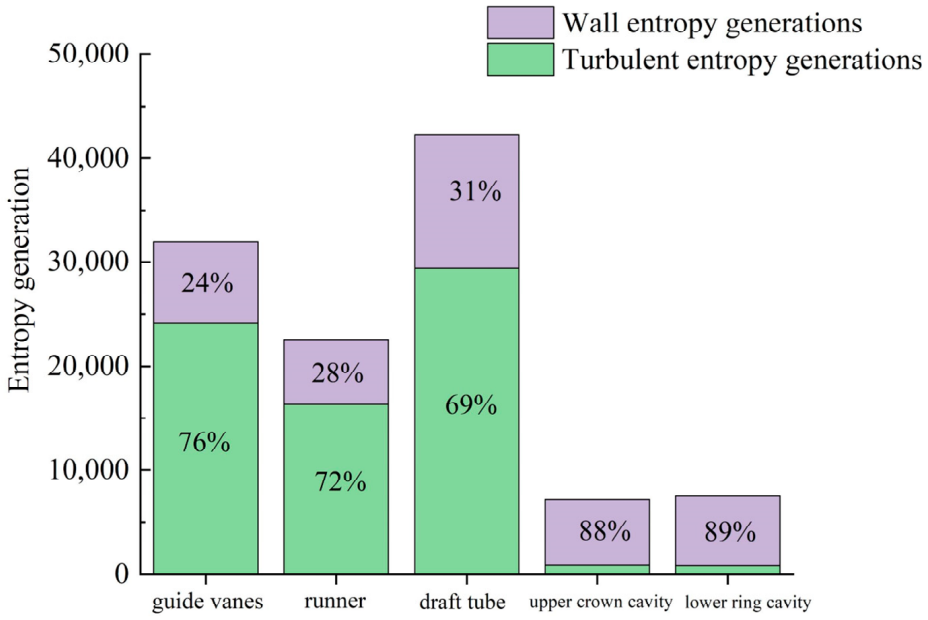

Figure 5. Different types of entropy output value and its proportion.

The guide vanes, runners, and draft tubes are pivotal in the pump turbine's entropy generation process, with the hydraulic losses they induce significantly impacting the overall performance of the turbine unit. As depicted in Figure 4, the entropy production

in these three components constitutes an overwhelming majority of the total entropy output. Consequently, a thorough analysis of entropy production for the guide vanes, runners, and draft tubes will be conducted in the subsequent sections to further elucidate their contributions to the system's hydraulic efficiency and identify potential areas for optimization.

3.2. Hydraulic Loss and Internal Flow Characteristics of Guide Vane and Runner Parts

Guide vanes and runners represent the most critical hydraulic components within the turbine unit, with their operational status being directly linked to the efficiency of energy transformation. To pinpoint the principal zones of energy dissipation, an entropy generation analysis is initially conducted on the wall surfaces. Subsequently, this analysis is expanded to scrutinize the conditions within the flow channels, ensuring a comprehensive evaluation of the areas contributing most significantly to hydraulic losses.

Figure 6 illustrates the distribution of wall entropy production (WEPR) across the guide vane and runner regions. The visualization reveals an increasing trend of entropy generation in areas from the vaneless space towards the fixed guide vane's flow path. Particularly, high concentrations of WEPR are observed in the vaneless region between the guide vane and the runner, and along the trailing edge of the movable guide vane. Correlation with the velocity field imagery indicates that the significant velocity gradients due to the high-velocity flow in the vaneless area are the main contributors to the elevated WEPR.

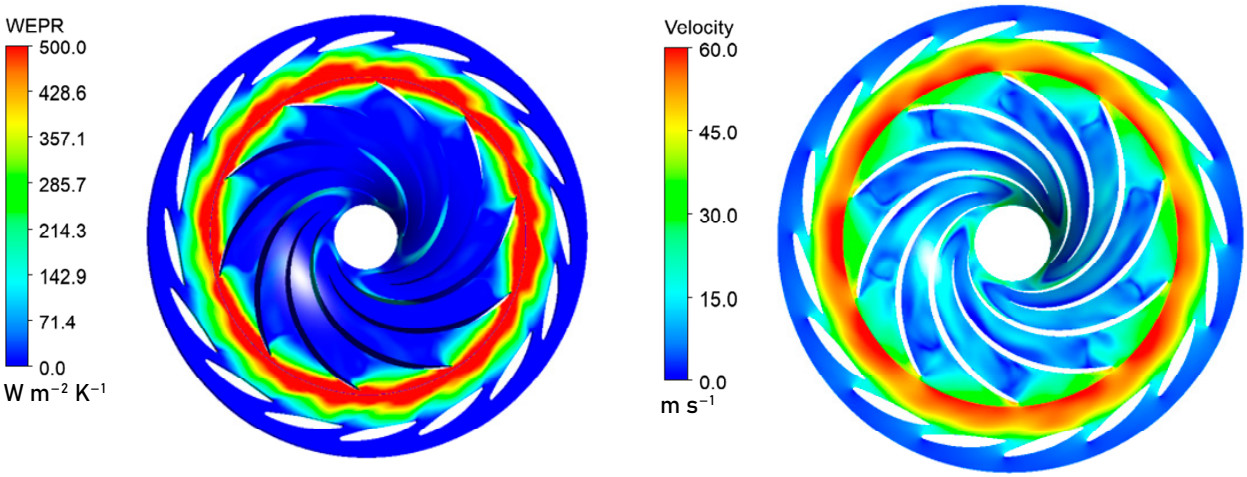

Figure 6. Wall entropy production distribution of guide vane and runner region.

The entropy generation analysis within the flow channel is conducted subsequent to the extraction of three runner surfaces, each oriented at different spanwise positions, through a blade-to-blade approach. The surfaces, labeled as Span 0.1, Span 0.5, and Span 0.9, are progressively documented from the upper crown to the lower ring of the runner, as shown in Figure 7. The analysis indicates a rising trend in entropy production along the runner channel, with the Local Entropy Production Rate (LEPR) being significantly higher near the upper crown flow surface than it is near the lower ring flow surface.

Notable LEPR is primarily detected at the leading and trailing edges of the runner blades. This phenomenon is largely due to the misalignment between the angle of the incoming flow at the runner's inlet and the designed inlet angle of the blades. The misalignment causes the incoming flow to exert a substantial impact on the leading edge, leading to local backflow and consequently a pronounced level of hydraulic loss. Additionally, the trailing edge of the blade experiences varying degrees of flow separation, creating a significant velocity gradient and resulting in energy dissipation.

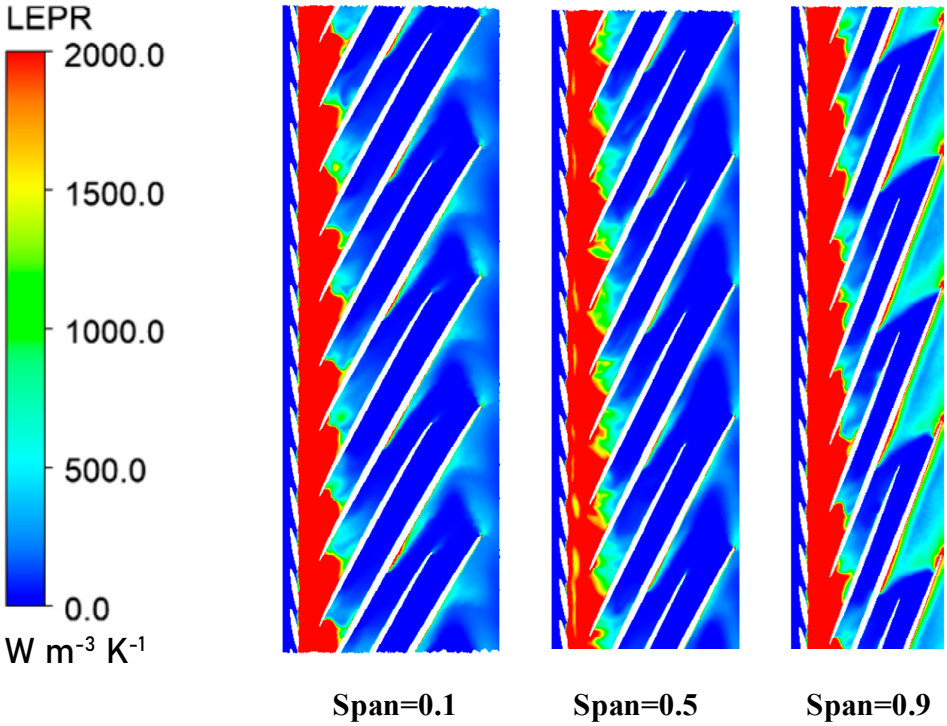

Figure 7. Analysis of entropy generation in runner channel.

This nuanced analysis underscores the importance of blade design and the need to consider the interaction between the flow angle and blade geometry to minimize energy losses and optimize turbine performance. In conclusion, the regions experiencing significant energy loss within the guide vane and runner areas have been identified, setting the stage for a more detailed analysis of the flow dynamics within the runner area. Figure 8 depicts the streamline distribution within the guide vane and runner area at four critical torque instances during a cycle. The streamline pattern reveals the non-uniformity within the runner, particularly at the inlet where the swift water flow creates a high-velocity ring in the vaneless space, encircled by numerous vortices. This occurrence is partly due to the dynamic and static interferences—namely, the uneven flow velocities and directional changes at the guide vane outlet exert a periodic influence on the runner's inlet boundary conditions. Such periodic fluctuations induce instability within the runner's internal flow, leading to the formation of vortices and flow separation. Sustaining this unstable flow condition results in substantial energy dissipation and an increase in hydraulic losses within the runner.

Figure 9, which presents the distribution of turbulent kinetic energy, allows for a deeper comprehension of how flow instability contributes to hydraulic losses. The higher values of turbulent kinetic energy, as depicted, are predominantly found in the vaneless area and at the interface between the guide vane channel and the runner channel, aligning with the high-velocity water ring and vortex phenomena observed. Furthermore, a localized peak in turbulent kinetic energy is evident near the inlet on the pressure side of the runner blade, suggesting that flow separation occurs in this region. This separation is a direct contributor to local hydraulic losses.

To delve deeper into the impact of dynamic and static interferences on hydraulic losses within the runner area, Figure 10 examines the local velocity vectors of both the runner and the guide vane.

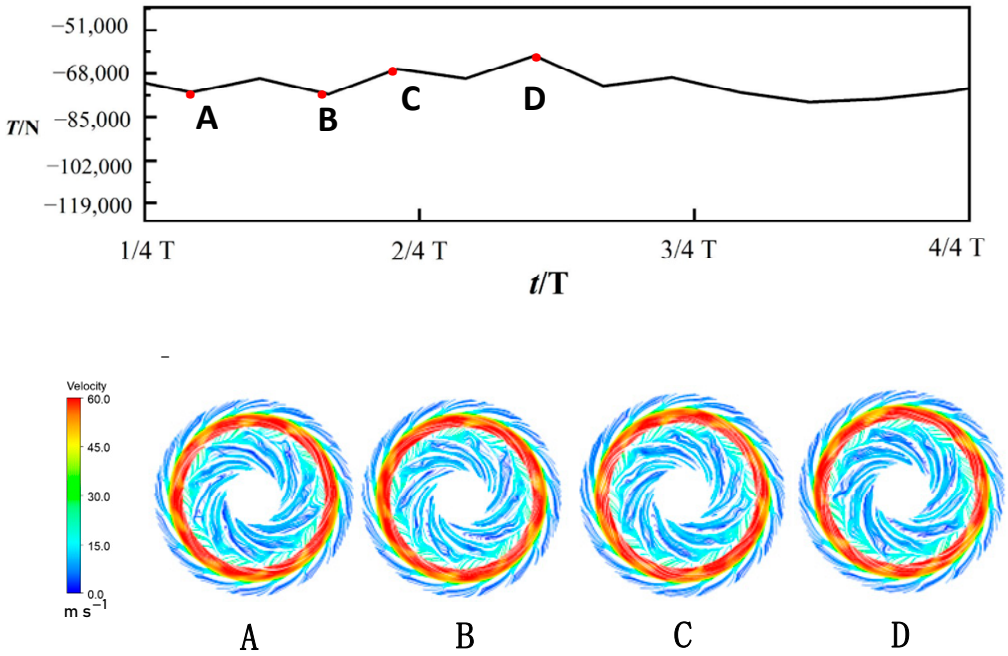

Figure 8. The streamline distribution of the guide vane and runner area.

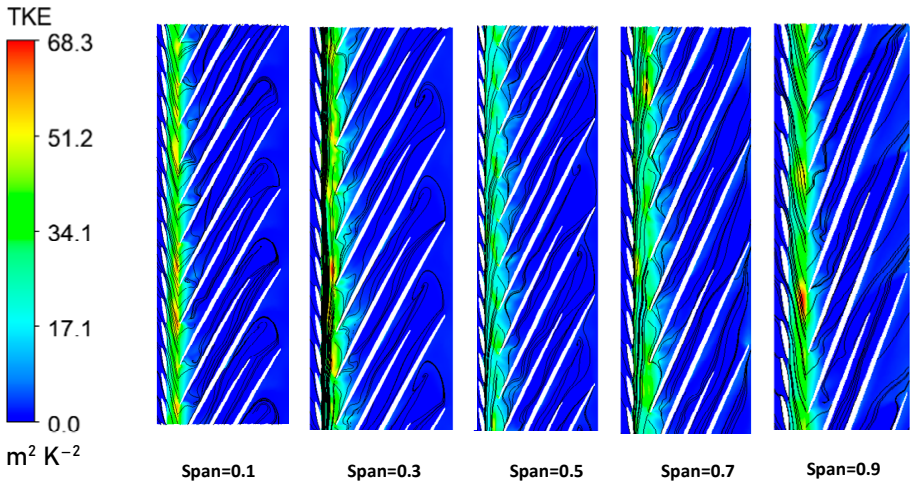

Figure 9. Distribution of turbulent kinetic energy in runner channel.

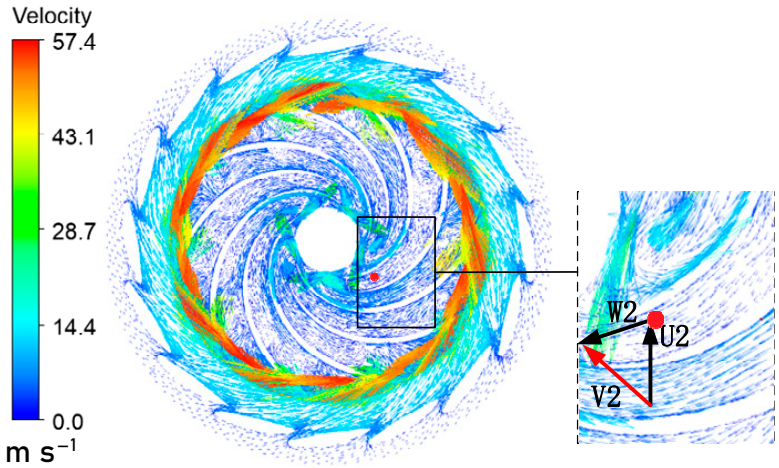

Figure 10. Local velocity vector of runner and guide vane.

It is noted that the water flow at the runner's inlet possesses a notably high circumferential velocity. Upon entering the runner, this flow exerts a strong impact on the leading edge of the blade's suction surface, leading to flow separation. A portion of the water flow is deflected towards the pressure surface side, where its velocity is markedly decreased. Driven by a substantial centrifugal force, this segment of the flow is ejected towards the inlet direction, interacting with the incoming flow on the suction surface side and creating a large-scale vortex that obstructs the flow channel. Along the flow direction, the flow separation and backflow phenomena are filled in each spanwise surface, resulting in further deterioration of the flow pattern. Such occurrences are direct outcomes of rotor–stator interactions, as the non-uniform velocity distribution at the guide vane outlet leads to intricate flow patterns within the runner, characterized by flow separation and reverse flow. An analysis of the runner blade's velocity triangle reveals that the absolute velocity V2 direction at the runner outlet aligns with the direction of the traction velocity U2. Consequently, the water flow at the draft tube inlet will form a helical vortex belt under the influence of positive velocity circulation.

To delve deeper into the vortex structures within the runner and guide vane, Figure 11 presents a vorticity distribution map of the runner throughout a cycle.

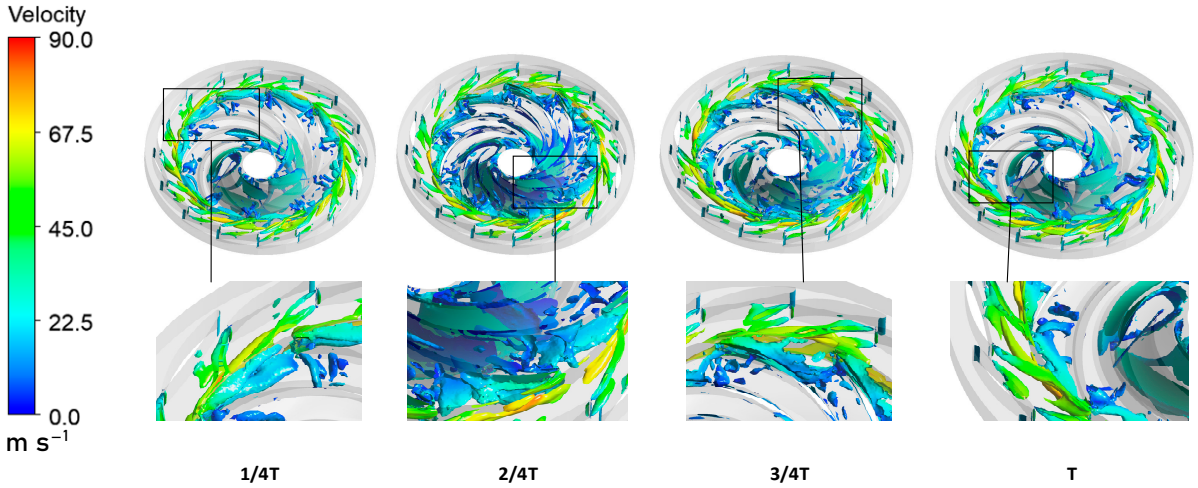

Figure 11. The vorticity distribution diagram of the runner in one cycle.

Most vortices are found near the intake of the runner blade's suction surface. Also, a vortex region is detected at the outlet's trailing edge on the pressure side of the extended blade. The water flow's influence on the suction side of the extended blade at the inlet results in lateral or reverse flow, thus generating a passage vortex. A distinctive horseshoe-shaped vortex is observed along the inner wall of the runner. High-velocity water circulation passing through the inner side of the guide vane carries away numerous smaller streamwise vortices from the upper and lower end walls. These vortices coalesce with the existing streamwise vortices at the runner's inlet, evolving into larger-scale vortices, the positioning of which correlates with the runner blade's orientation.

Drawing from the analysis presented in Figures 9 and 10, it is evident that the rotor-stator interaction exerts influence over not only the velocity vectors and flow separation within the runner area but also directly contributes to the emergence of intricate vortex structures within the runner and guide vane. The presence of these vortex formations further amplifies hydraulic losses, thereby impacting the pump turbine's efficiency and operational stability. The periodic flow separation and the genesis of vortex structures, instigated by dynamic and static interference, induce pressure fluctuations along the flow channel. Consequently, the pressure pulsations within the runner section will be examined in the subsequent analysis. To convey the nature of pressure pulsations more vividly,

this study introduces the dimensionless pressure pulsation coefficient Cp to denote the magnitude of pressure oscillations. The precise formula is presented below:

$$C_{p=}\frac{P-\overline{P}}{\frac{1}{2}\rho u_2^2} \tag{17}$$

In the formula: P signifies the instantaneous pressure at the monitoring point; $\overline{P}$ denotes the time-averaged pressure at the monitoring point over a specified period; ρ is the water density; u_2 is the linear velocity at the turbine runner's inlet.

Initially, pressure readings from various monitoring points are collected and subsequently transformed into pressure fluctuation coefficients Cp to create time-domain signals. Subsequently, these time-domain signals are translated into the frequency domain using Fast Fourier Transform (FFT), yielding both time-domain and frequency-domain plots for each monitoring location, as depicted in Figure 12.

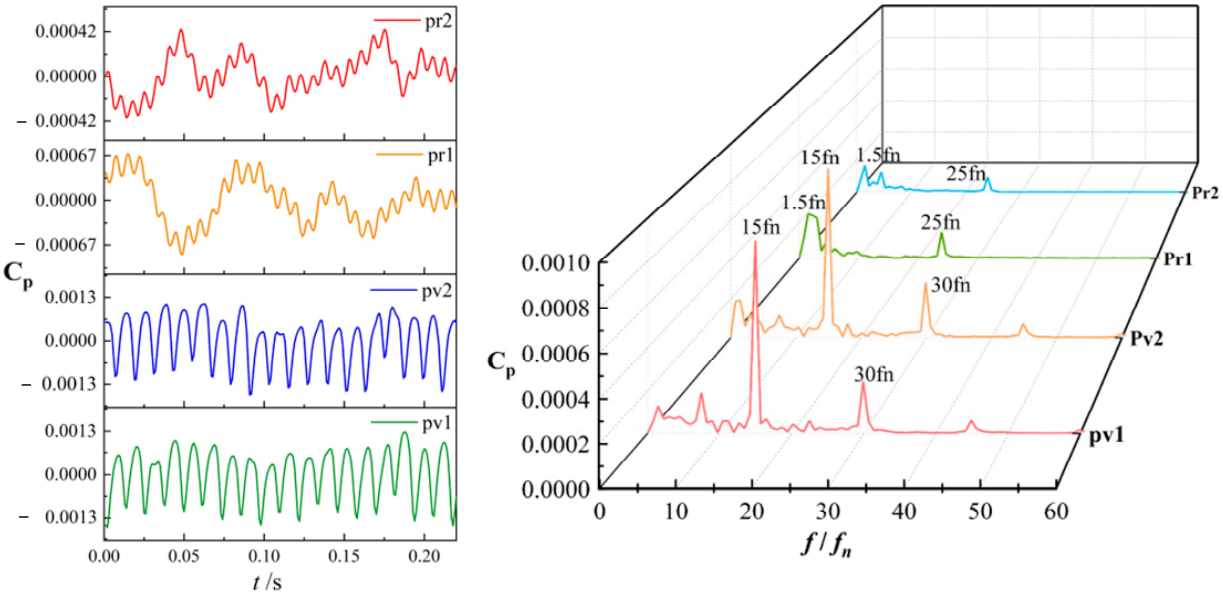

Figure 12. The time-domain and frequency-domain plots for the monitoring points within the runner and guide vane regions.

The time-domain pattern of pressure pulsations in the vaneless area displays a clear periodicity, in contrast to the less distinct pattern observed at the runner. Examination of the frequency domain indicates that the main frequency of pressure pulsation in the vaneless area is at 15 fn (with fn being the shaft frequency), aligning with the passing frequency of the stay vane and classified as a high-frequency pressure pulsation element. These pressure pulsations at this frequency are largely attributed to the dynamic and static interactions between the movable guide vane and the runner. In the frequency domain diagram, alongside the primary frequency of 15 fn, another notable frequency is the shaft frequency multiplication. At the runner, the principal frequency of pressure fluctuation is 1.5 fn, with a concurrent surge in frequency at 25 fn, indicating a significant impact from dynamic and static interference. These observations underscore the complex interactions within the turbine that contribute to pressure pulsations and their influence on the system's hydraulic.

In the frequency domain analysis, in addition to the primary frequency at 15 fn, another significant frequency is the multiplication of the shaft frequency. At the runner, the predominant frequency of pressure fluctuation is 1.5 fn, with a notable increase at 25 fn, suggesting a substantial effect from dynamic and static interference. These findings

highlight the intricate interactions within the turbine that are responsible for pressure pulsations and their consequential effects on the system's hydraulic performance.

3.3. Hydraulic Loss and Internal Flow Characteristics of Draft Tube

As an essential element of the pump turbine, the draft tube's internal flow dynamics substantially influence the overall performance of the system. The subsequent section presents an entropy generation analysis focusing on the hydraulic losses within the draft tube.

Figure 13 illustrates the distribution of wall entropy generation and direct entropy generation within the draft tube.

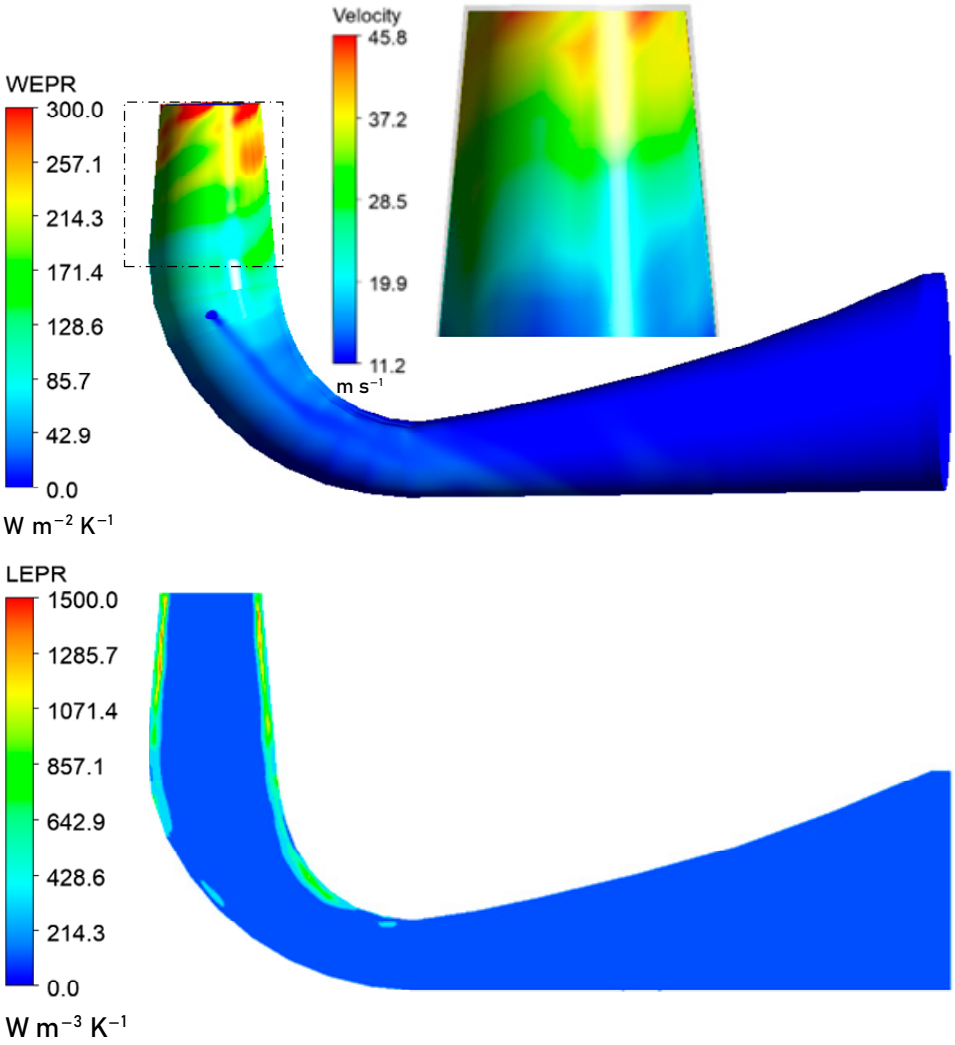

Figure 13. Distribution of wall entropy generation and direct entropy generation of draft tube.

Observations indicate that the area of elevated entropy generation extends downward from the straight conical section of the draft tube, with fluid velocities exhibiting a gradual increase from the core to the periphery. This trend could be associated with the fluid's viscous behavior and the evolution of the turbulent boundary layer adjacent to the wall. As the fluid progresses through the straight conical section, the velocity gradient intensifies near the wall, leading to heightened wall shear stress. Within the central region of the straight conical segment, a pronounced acceleration of fluid velocity along the wall is noticeable. The majority of the high wall entropy production rate (WEPR) is concentrated in this straight conical section, with the primary hydraulic losses in the draft tube attributable to vortex band formation and flow complexity. Vortices are a principal driver

of hydraulic vibrations in pump turbines. During no-load operation, these vortices can induce substantial pressure fluctuations and consequent whole-unit vibrations within the draft tube.

To delve deeper into the origins of elevated entropy production within the draft tube, Figure 14 presents a cross-sectional cloud diagram of velocity and turbulent kinetic energy from the straight cone section to the draft tube's outlet.

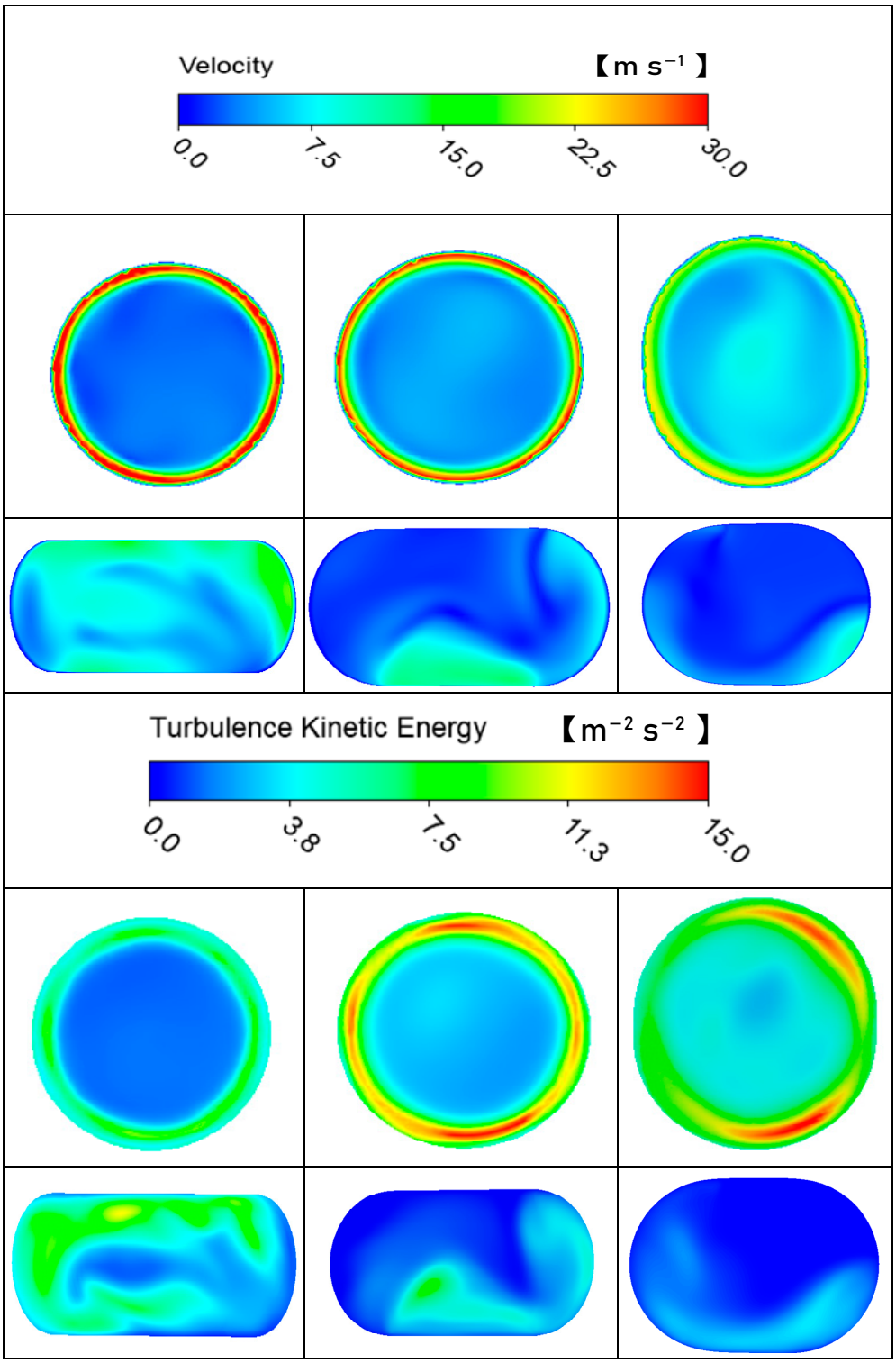

Figure 14. The cross-sectional cloud diagram of velocity and turbulent kinetic energy in the draft tube, spanning from the straight cone section to the outlet.

Observations reveal a similar pattern in the distribution of entropy production, with fluid velocities and turbulent kinetic energy exhibiting a gradual increase moving from the center towards the wall. The progression of flow velocity aligns closely with the escalation of turbulent kinetic energy. This is because high turbulent kinetic energy means that there are more velocity fluctuations in the fluid, which may lead to more effective momentum and energy transfer, thus affecting fluid diffusion and heat transfer characteristics.

In conclusion, the flow conditions at the draft tube inlet seem to be less than ideal, likely a consequence of static and dynamic interference. The flow behavior within the draft tube is shaped by the interplay between the stationary wall and the fluid in motion, potentially leading to flow separation, vortex formation, and increased turbulence. To gain further insights into the draft tube's internal flow characteristics, Figure 15 depicts the internal vortex and streamline configurations:

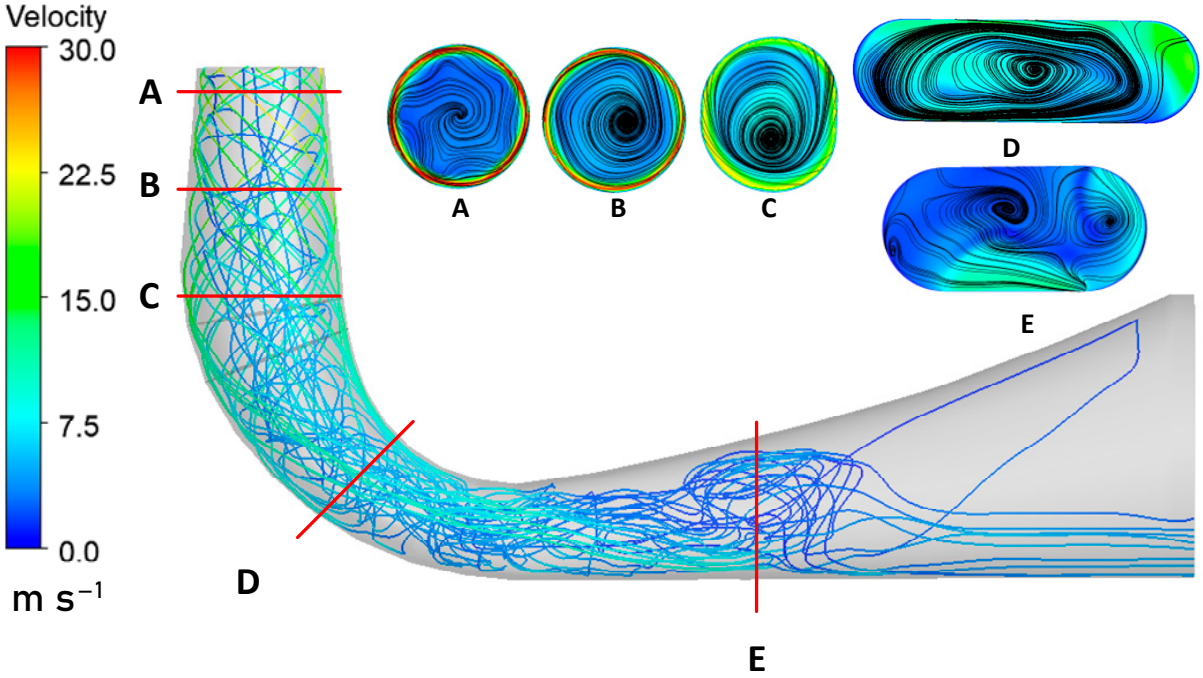

Figure 15. Vortex and streamline distribution in draft tube.

Sections A, B, and C are situated in the vicinity of the draft tube inlet within the straight cone section, section D is located in the elbow region, and section E is within the horizontal diffuser section. It is apparent that during no-load operations, the flow becomes notably more chaotic, with helical vortex bands developing in both the straight cone and elbow sections of the draft tube, and isolated, scattered vortices appearing in the horizontal diffusion section. The arrangement of streamlines and vortices suggests that the flow within the draft tube is markedly unstable under such circumstances, contributing to significant hydraulic losses.

The periodic flow separation and vortex structure formation, instigated by dynamic and static interference, induce pressure fluctuations within the flow channel. The pressure pulsations in the draft tube will be examined next. Employing the same research methodology as for the runner, the time-domain and frequency-domain plots for each monitoring point are derived, as illustrated in Figure 16.

The time-domain distribution of pressure pulsations at the draft tube inlet's straight cone section exhibits clear periodicity, whereas the pressure pulsations in the elbow section display a less pronounced pattern. Notably, the elbow section shows six peaks across three rotation cycles. The pressure pulsation components within the draft tube are intricate, with internal flow anomalies generating a potent stochastic pressure signal. In addition to frequencies associated with dynamic and static interference, the pressure

pulsation spectra at each measurement point also encompass numerous low-frequency, high-amplitude components.

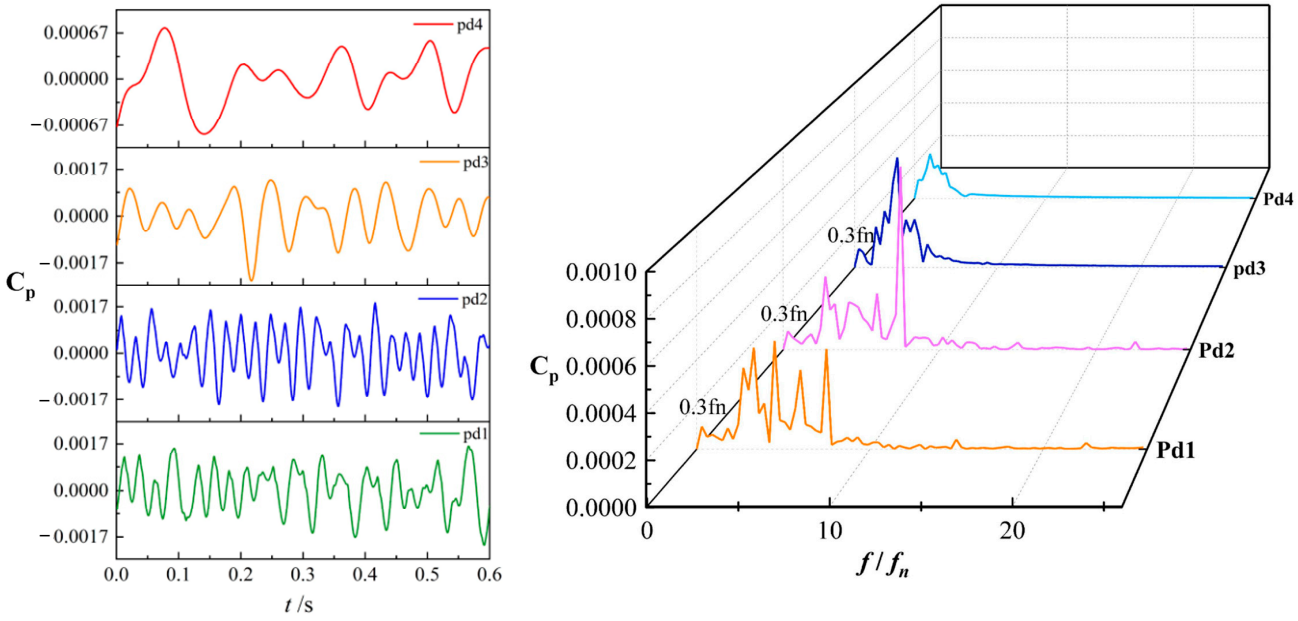

Figure 16. The time-domain and frequency-domain plots for the monitoring points located within the draft tube.

4. Conclusions

In this research, numerical simulations were conducted on the pump turbine at Weifang Pumped Storage Power Station with the guide vanes set to a constant opening under no-load conditions. The key findings are as follows:

(1) Under no-load conditions, the system's entropy generation is predominantly driven by turbulent fluctuations and wall effects. Turbulent and wall entropy generations collectively constitute the majority of the total entropy production, surpassing 99%, with direct entropy generation contributing less than 1%. The predominant hydraulic losses are identified in the regions of the guide vane, runner, and draft tube.

(2) The runner's internal flow is characterized by non-uniformity and disorder across flow channels, with numerous vortices obstructing the flow path. High-velocity flow regions, predominantly in the vaneless space, stem from the dynamic and static interactions between the runner and stationary elements. The draft tube experiences considerable flow instability, characterized by the formation of spiral vortex bands in the straight cone and elbow sections, and the emergence of discrete vortices in the horizontal diffusion section, which contribute to substantial hydraulic losses.

(3) The primary frequencies of pressure pulsation within the runner and vaneless area are fundamentally 25 and 15 times the shaft frequency, indicating that dynamic and static interference is a major factor in pressure pulsation. The bladeless region exhibits the greatest amplitude of main frequency, where dynamic and static interference is most pronounced. The pressure pulsation components in the draft tube are intricate, reflecting the complex interplay of forces within the system and underscoring the need for detailed analysis and optimization to enhance performance and stability.

Author Contributions: Conceptualization, Methodology and Writing—original draft, X.L. (Xianliang Li); Software, H.D.; Writing—review & editing, Y.L.; Formal analysis, X.L. (Xiji Li); Supervision, Z.W. All authors have read and agreed to the published version of the manuscript.

Funding: The authors declare that financial support was received for the research, authorship, and/or publication of this article. This study was supported by the Science and Technology Project of State Grid Xinyuan Group Company Limited (Contract No. SGXYK-2023-117), the Joint Open Research Fund Program of the State Key Laboratory of Hydroscience and Engineering the and Tsinghua-Ningxia Yinchuan Joint Institute of the Internet of Waters on Digital Water Governance (sklhse-2024-ow07), Natural Science Foundation of Jiangsu Province (BK20210771).

Data Availability Statement: Data is contained within the article.

Conflicts of Interest: Authors Haiyang Dong, Xiji Li were employed by the company State Grid Xinyuan Shandong Weifang Pumped Storage Co., Ltd. The remaining authors declare that the research was conducted in the absence of any commercial or financial relationships that could be construed as a potential conflict of interest.

References

1. Chang, Y.H.; Gui, Z.H.; Lu, W.F.; Fan, L.N.; Lu, Z.H. Status Analysis of the Study on the Stability of Pumped Storage Unit with No-load. *Hydropower Pumped Storage* **2016**, *2*, 70–75.
2. Gentner, C.; Sallaberger, M.; Widmer, C.; Bobach, B.-J.; Jaberg, H.; Schiffer, J.; Senn, F.; Guggenberger, M. Comprehensive experimental and numerical analysis of instability phenomena in pump turbines. *IOP Conf. Ser. Earth Environ. Sci.* **2014**, *22*, 32046. [CrossRef]
3. Houde, S.; Dumas, G.; Deschênes, C. Experimental and numerical investigations on the origins of rotating stall in a propeller turbine runner operating in no-load conditions. *J. Fluids Eng.* **2018**, *140*, 111104. [CrossRef]
4. Li, X.; Cao, J.; Zhuang, J.; Wu, T.; Zheng, H.; Wang, Y.; Zheng, W.; Lin, G.; Wang, Z. Effect of operating head on dynamic behavior of a pump-turbine runner in turbine mode. *Energies* **2022**, *15*, 4004. [CrossRef]
5. Decaix, J.; Hasmatuchi, V.; Titzschkau, M.; Münch-Alligné, C. CFD Investigation of a High Head Francis Turbine at Speed No-Load Using Advanced URANS Models. *Appl. Sci.* **2018**, *8*, 2505. [CrossRef]
6. Nennemann, B.; Morissette, J.F.; Chamberland-Lauzon, J.; Monette, C.; Braun, O.; Melot, M.; Coutu, A.; Nicolle, J.; Giroux, A.M. Challenges in dynamic pressure and stress predictions at no-load operation in hydraulic turbines. *IOP Conf. Ser. Earth Environ. Sci.* **2014**, *22*, 032055. [CrossRef]
7. Jiang, A.; Kong, L.; Zhang, T.; Tan, X.; Tan, H.; Guo, H.; Ren, S.; Yang, Q. Comprehensive experimental and numerical analysis of the strength and modal characteristics of the runner in a large pumped storage power station pump-turbine. *Hydropower Pumped Storage* **2023**, *9*, 19–24.
8. Wang, R.B. Comprehensive Study on the Startup Transient Process of Reversible Pump-Turbines. Master's Thesis, Lanzhou University of Technology, Lanzhou, China, 2018.
9. Meng, Q. Research on the Dynamic Characteristics and Internal Flow Mechanism of Pump-Turbines during the Transition Process in the S-Characteristic Area. Ph.D. Thesis, Lanzhou University of Technology, Lanzhou, China, 2020.
10. Hu, J.H. Research on the S-Characteristics and Pressure Pulsation Control of Pump-Turbines. Ph.D. Thesis, Wuhan University, Wuhan, China, 2021.
11. Huang, W.; Bi, H.; Ye, Y.; Zhang, S.; Yin, X.; Huang, X.; Wang, Z.; Jin, Z. Comprehensive study on the hydraulic characteristics during the startup process of pump-turbines. *J. Hydroelectr. Eng.* **2023**, *42*, 97–104.
12. Liang, A.; Li, H.; Zhang, W.; Yao, Z.; Zhu, B.; Wang, F. Study on pressure fluctuation and rotating stall characteristics in the vaneless space of a pump-turbine in pump mode. *J. Energy Storage* **2024**, *94*, 112385. [CrossRef]
13. Hu, L.; Liang, A.; Li, H.; Zhang, W.; Zhu, B. lmpact of rotor-stator axial spacing on the gas-liquid-solid flow characteristics of a multiphase rotodynamic pump based on the Euler multi-fluid model. *Phys. Fluids* **2024**, *36*, 063314. [CrossRef]
14. Li, D.; Zhang, N.; Jiang, J.; Gao, B.; Alubokin, A.A.; Zhou, W.; Shi, J. Numerical investigation on the unsteady vortical structure and pressure pulsations of a centrifugal pump with the vaned diffuser. *Int. J. Heat Fluid Flow* **2022**, *98*, 109050. [CrossRef]